

Formation of Multifractal Population Patterns from Reproductive Growth and Local Resettlement

Jonathan Ozik*

*Department of Physics and Institute for Research in Electronics and Applied Physics,
University of Maryland, College Park, Maryland 20742*

Brian R. Hunt

*Department of Mathematics and Institute for Physical Science and Technology,
University of Maryland, College Park, Maryland 20742*

Edward Ott

*Department of Physics, Department of Electrical and Computer Engineering,
and Institute for Research in Electronics and Applied Physics,
University of Maryland, College Park, Maryland 20742*

(Dated: December 2, 2024)

Abstract

We consider the general character of the spatial distribution of a population that grows through reproduction and subsequent local resettlement of new population members. Several simple one and two-dimensional point placement models are presented to illustrate possible generic behavior of these distributions. It is shown, numerically and analytically, that these models all lead to multifractal spatial distributions of population. Additionally, we make qualitative links between our models and the example of the Earth at Night image [1], showing the Earth's nighttime man-made lights as seen from space. The Earth at Night data suffer from saturation of the sensing photodetectors at high brightness ('clipping'), and we account for how this influences the determined multifractal dimension spectrum of the light intensity distribution.

*Electronic address: jozik@umd.edu



FIG. 1: A version of the Earth at Night image [1]. This is a composite image created with data from the Defense Meteorological Satellite Program of the Earth's nighttime man-made lights as seen from space. For the analysis, an 8-bit grayscale 2400x800 pixel image was used, where light from the reflective landmasses found in the original image was removed with an appropriate uniform background subtraction. The image pixels have intensity values ranging from 0 to 218.

I. INTRODUCTION

Growing populations exist in many different areas of interest. Although the most obvious examples are biological in nature (e.g., bacterial cultures, the human population), one can also consider the growth of technological development or the growth of urban infrastructure as more abstract examples. While the specific details of these systems can be quite different, the examples stated here all share the characteristic that their populations grow on some background space. A reasonable question to ask then is what types of spatial distributions result in these growing systems. Figure 1 is a version of the popular Earth at Night image (EaN) [1]. This is a composite image taken by orbiting satellites that shows the Earth's nighttime man-made lights as seen from space. The light intensities are brightest in areas that are known to be highly populated and developed, and thus the image can be crudely thought of as representing the spatial distribution of some combined measure of technological development and human population density. We see a very heterogeneous distribution, with areas of very high intensities as well as areas of almost no light at all.

A useful characterization of the heterogeneity of a distribution is the distribution's *dimension spectrum* D_q . A grid of hypercubes, or boxes, of a fixed size with edge length ϵ is used to cover the distribution, where the dimension of the hypercubes corresponds to the

dimension of the underlying space (e.g., squares for two dimensions and line segments for one dimension). D_q is then calculated via [2, 3]

$$D_q = \frac{1}{1-q} \lim_{\epsilon \rightarrow 0} \frac{\ln I(q, \epsilon)}{\ln(1/\epsilon)}, \quad (1)$$

where

$$I(q, \epsilon) = \sum_{i=1}^{N(\epsilon)} \mu_i^q. \quad (2)$$

Here the sum is taken over $N(\epsilon)$ non-empty grid boxes and μ_i is the fraction of the particular quantity of interest (assumed to be nonnegative, e.g., light intensity in Fig. 1) that is contained in box i .

The parameter q ($q \geq 0$ in this paper) can be varied continuously to vary the influence of high and low μ_i boxes, with larger values of q emphasizing the boxes with larger μ_i 's. In particular, when $q = 1$ we have the *information dimension* D_1 which, applying L'Hospital's Rule to (1) and (2), is given by

$$D_1 = \lim_{\epsilon \rightarrow 0} \frac{\sum_{i=1}^{N(\epsilon)} \mu_i \ln \mu_i}{\ln \epsilon}. \quad (3)$$

A distribution is *fractal* if it possesses a fractional (non-integer) dimension (i.e., if D_q is not an integer for some q). If D_q depends on q , then the distribution is said to be *multifractal*.

Generally, when measuring the dimension of a distribution of numerical and/or experimental data, there is a maximum resolution observable. In the EaN image, for example, the image's individual pixels are the smallest boxes that can be used to cover the distribution in the calculation of D_q . In such cases the $\epsilon \rightarrow 0$ limit cannot be considered; instead one looks for a *scaling range* of ϵ where the quantity $(1-q)^{-1} \ln I(q, \epsilon)$ varies approximately linearly with $\ln(1/\epsilon)$, from which a dimension can be extracted as the slope of a straight line fitted to data in the ϵ scaling range. We illustrate this process by calculating the information dimension D_1 of the EaN image. Figure 2 shows a plot of $\sum_{i=1}^{N(\epsilon)} \mu_i \ln \mu_i$ versus $\ln \epsilon$ (with ϵ in units of pixels) for the image, where each μ_i is the fraction of the total intensity in box i . The good evidence of linearity in this plot over a scaling range in ϵ of order e^6 indicates that a fractal description makes sense. The solid line in Fig. 2 is a linear fit to the data with a slope of 1.60 ± 0.02 , which we take as the value of D_1 . Thus the light distribution in the EaN is fractal. In Sec. III we argue that it is also multifractal.

Yook et al. [4] have recently reported that the world's human population, as well as the population of internet routers and autonomous systems, are fractally distributed. Ad-

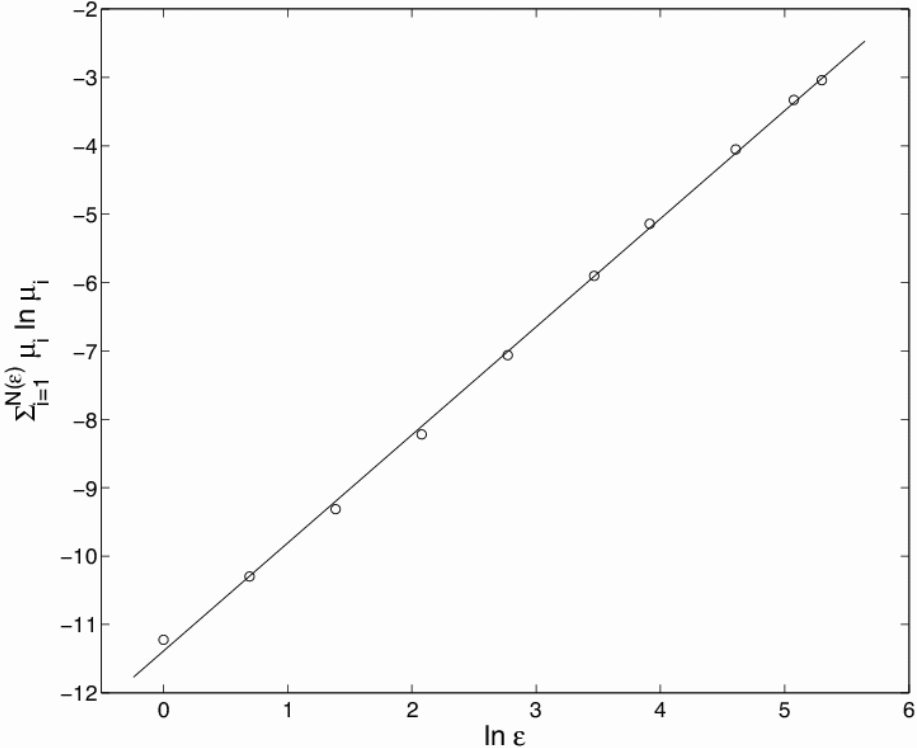


FIG. 2: Plot for calculating the information dimension D_1 [see Eq. (3)] for the Earth at Night image. The quantity $\sum_{i=1}^{N(\epsilon)} \mu_i \ln \mu_i$ is plotted versus $\ln \epsilon$ (open circles), where ϵ is in units of pixels, resulting in a linear *scaling region*, the slope of which is a finite-scale approximation of D_1 . The solid line is a linear fit to the data with a slope of 1.60 ± 0.02 .

ditionally, several studies [5, 6, 7] have demonstrated various fractal properties of urban settlements. We were thus led to consider the possibility of common, underlying mechanisms shared by growing populations that lead to fractal distributions.

One characteristic found in many growing populations is the existence of some generalized reproduction process, where existing members of the population generate more members. In addition to biological reproduction, in some non-biological systems concentrated populations can encourage the creation of more members. For example, areas that are technologically highly developed are likely to stimulate more development than areas that are not as technologically developed.

Once the new members are generated, it is reasonable to expect some form of local resettlement for a wide range of growing systems. The resettlement is necessary in populations where individual members are unable to occupy the same physical space as other members.

In this paper we demonstrate that these two ingredients, reproduction and local resettlement, can lead to multifractal spatial distributions for growing populations. We present several point placement models in one and two dimensions which implement these ideas and show, both numerically and analytically, that they lead to multifractal distributions.

One might suspect that fractal population densities arise due to strong inhomogeneities of the underlying space (e.g., inhomogeneities in the distribution of land fertility, natural resources, etc.). Our models initially (Sec. II) employ spaces that have *no inhomogeneity*, thus demonstrating that fractal population distributions can occur without inhomogeneity. We also consider generalizations to our models that include geographical inhomogeneities (Sec. IV) and demonstrate that, for the particular forms of the inhomogeneities that we employ, the multifractality of the distribution is unaffected.

In Sec. II we present our point placement models along with numerical results. (We emphasize that the set of models we introduce in Sec. II is not exhaustive, and many other similar models could be conceived.) Section III considers situations where a multifractal distribution is sensed by an instrument that saturates at a maximum measurable value (clipping). We show that such clipping occurs in the EaN data, affecting the determined D_q . In Section IV, we investigate the effect of adding geographical inhomogeneity to the underlying space of our models. In Sec. V we present analytical results for some of our models. We summarize our findings and conclude in Sec. VI. Appendix A provides details and background on the analytical calculation of the spectra of fractal dimensions for some of our models. Appendix B contains the proof of a theorem used in Appendix A (this theorem should be of very general utility, not restricted to our specific models, in analysis of the spectra of fractal dimensions).

II. MODELS AND RESULTS

A. 1-D Random Interval (Model 1)

We begin with a very simple model that places points on the unit interval ($0 \leq x \leq 1$). Our initial state is a single point at $x = 0.5$. At each subsequent discrete time step we place a new point according to the following prescription: (a) a target point, or “parent”, is chosen from all of the preexisting points with equal probability; (b) the new point, or “child”, is

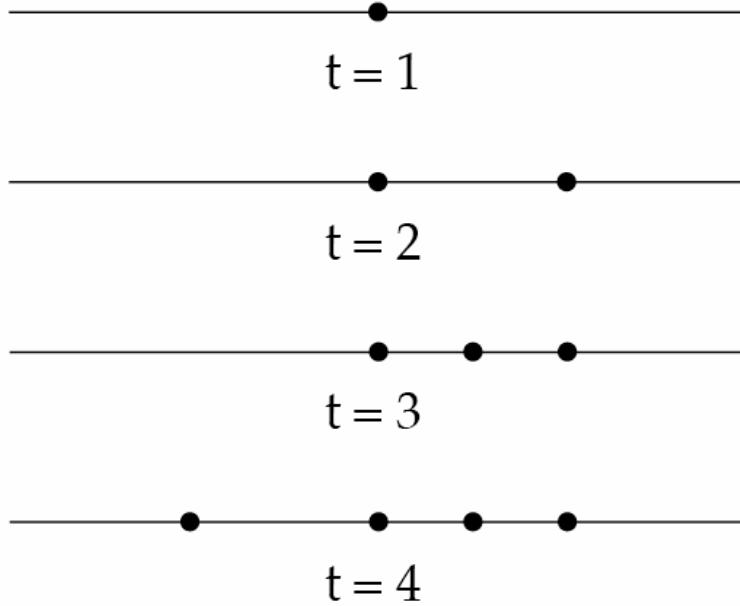


FIG. 3: Three representative steps of Models 1 and 3.

placed in the middle of one of the two empty intervals adjacent to the target point with equal probability. Steps (a) and (b) are repeated until the desired system size is reached. Several representative steps of this construction are illustrated in Fig. 3.

In Step (a), by randomly choosing the target point from all available preexisting points with equal probability, we allow every point to generate, attract, or reproduce new members at the same rate. This also implies that areas with a high density of points are more likely to attract new members than areas that are sparsely populated, creating a “rich get richer” phenomenon. We will see that all the models presented in this paper have this general characteristic, with most of the models actually possessing the identical Step (a). Step (b), on the other hand, is the local resettlement scheme that is particular to this model. It was chosen for its simplicity, and we will show in Sec. V A that analytical results can be obtained for it.

Figure 4 shows semilog plots of point location histograms with different bin sizes Δx for one realization of our point placement scheme. We observe a roughening of the plot as smaller histogram bins are used, thus giving a sense of the heterogeneity of the distribution. To quantify this heterogeneity, we calculate the dimension spectrum D_q of the distribution. We cover the distribution of points with intervals of a fixed length ϵ and assign to each

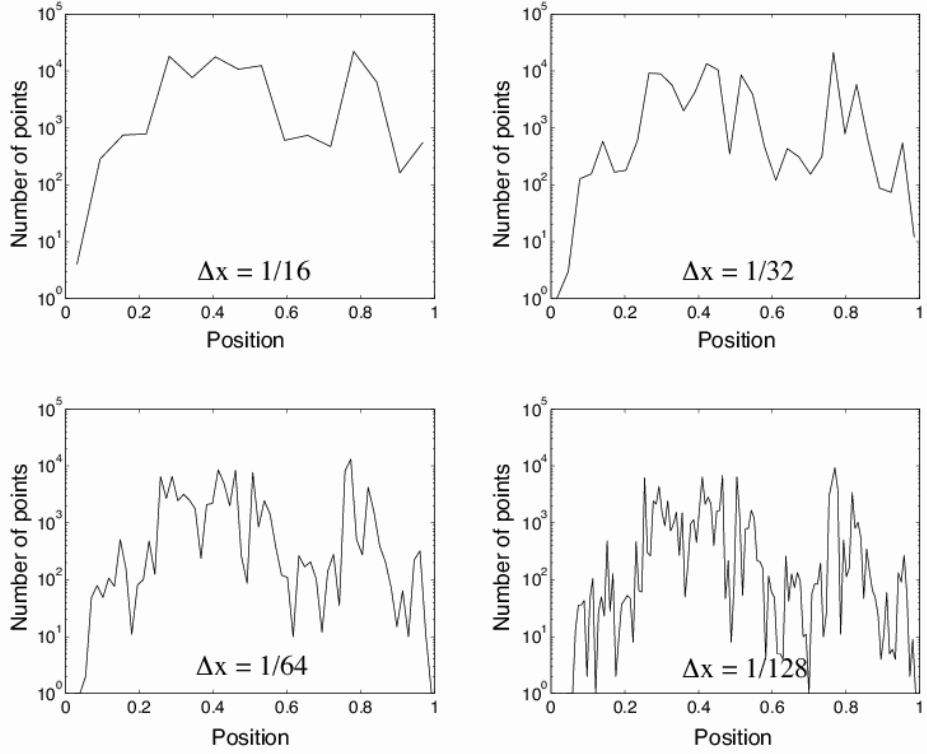


FIG. 4: Semilog plots of histograms of point locations on the unit interval for a 10^5 point distribution generated by Model 1, for various bin sizes Δx . a) $\Delta x = 1/16$, b) $\Delta x = 1/32$, c) $\Delta x = 1/64$, d) $\Delta x = 1/128$.

interval i a measure μ_i equal to the fraction of the total points contained in i . Then, referring to Eq. (1), we plot the quantity $(1 - q)^{-1} \ln I(q, \epsilon)$ versus $\ln(1/\epsilon)$ for a range of ϵ , so that the slope of the graph in the scaling range gives us D_q .

For $q \geq 0.5$ the plots exhibit a linear regime that allows for a relatively unambiguous determination of the dimension. However, for the smaller q there tend to be shorter scaling regions, which makes the extraction of a reliable D_q more error prone. This is due to the fact that the distribution is made up of a finite collection of points. As the grid covering the distribution is made finer, grid boxes in the more sparsely populated areas begin to contain either 0 or 1 points. Furthermore, if ϵ is made small enough, eventually all the points in the distribution are covered by different boxes, and the dimension for the distribution is simply the dimension of a collection of individual points, i.e., zero. Thus, in order to get a meaningful dimension out of a finite distribution of points, a certain degree of coarseness of the covering grid is necessary. For small values of q , D_q relies heavily on boxes containing

small amounts of the measure. Therefore, as ϵ is decreased, a scale is quickly reached where points in sparsely populated areas are covered by separate boxes, thereby destroying the overall scaling behavior. For larger q , the dense regions have a large enough influence on D_q that the effects of the finiteness of the distribution are not observed until very small scales are reached, allowing for a large scaling range.

Figure 5 is a plot of the numerically determined average D_q (open circles) for 20 realizations of 10^6 point distributions generated by Model 1. The solid line represents the analytical result for D_q derived in Sec. V A. Both the numerical and analytical results demonstrate that Model 1 generates multifractal distributions.

Notice that our analytical value for the box-counting dimension D_0 is one. Unlike D_q for q positive, D_0 depends only on the limiting set of points and not their distribution. Our result that $D_0 = 1$ indicates that the set filled by the points in Model 1 as time t goes to infinity is not fractal. In fact, the entire interval is filled with probability one, which we see as follows. At time t there are t points, which divide the unit interval into $t + 1$ subintervals (see Fig. 3). Each of the subintervals has probability $1/t$ of containing the next point, except for the two end subintervals, which each have probability $1/(2t)$. Thus the probability that a given subinterval is not bisected at time t is at most $1 - 1/(2t)$. Since the infinite product of these probabilities as $t \rightarrow \infty$ is zero, each subinterval is eventually bisected with probability one, and therefore no empty intervals remain as $t \rightarrow \infty$. One can similarly argue for the other models in this paper that the limiting sets are not fractal; the heterogeneous point distributions they yield are reflected by the fractional values of D_q for $q > 0$.

B. 2-D Random Square (Model 2)

Model 2 is a two dimensional analogue of Model 1, where points are placed on the unit square, $(0 \leq x \leq 1, 0 \leq y \leq 1)$, instead of the unit interval. We begin with a single point at $(0.5, 0.5)$. Imagining vertical and horizontal lines drawn through this point, we see that the point is at the vertex of four neighboring squares. At the next step, we choose one of the squares at random, with equal probability, and place a point in its middle. We then divide this chosen square into four smaller squares by horizontal and vertical lines through the newly added point. Then we continue this process: At each subsequent discrete time step we pick a target point (parent) according to Step (a) of Model 1 (that is, all points are

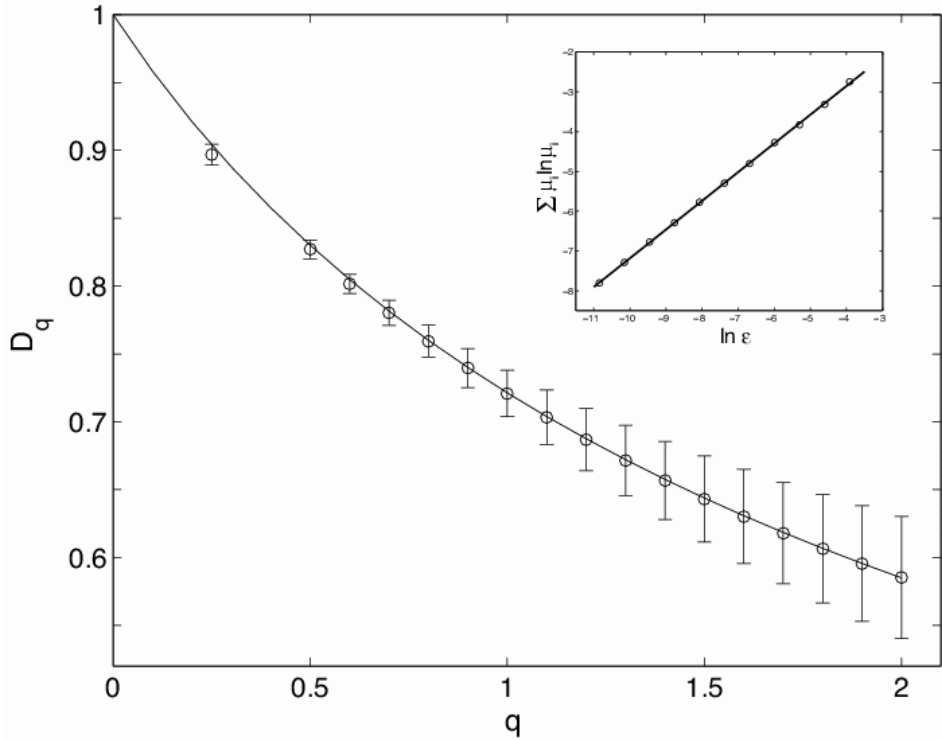


FIG. 5: Plot of D_q for Model 1. The open circles are the numerical values calculated from the slope of a line fit to $(1 - q)^{-1} \ln I(q, \epsilon)$ versus $\ln(1/\epsilon)$ [see Eq. (1)], averaged over 20 realizations of 10^6 point distributions (except for $q = 1$, in which case the line is fit to $\sum_{i=1}^{N(\epsilon)} \mu_i \ln \mu_i$ versus $\ln \epsilon$ [see Eq. (3)]), with the error bars indicating the sample standard deviation for each value. The solid line is the analytical result of Eq. (14). As an example the inset shows the determination of D_1 for one point distribution.

equally likely to be chosen) and add a new point (child) to the center of one of the target point's four adjacent squares, chosen with equal probability. Several representative steps of this construction are illustrated in Fig. 6.

Figure 7 shows a distribution generated by this model's point placement scheme, where we have successively magnified dense regions of the distribution to illustrate the large differences in densities that result at various length scales. Figure 8 is a plot of the average D_q of 20 independent distributions generated by this model, where the solid line is the analytical result (28) derived in Sec. V B. Again, both the numerical and analytical results confirm that Model 2 generates multifractal distributions.

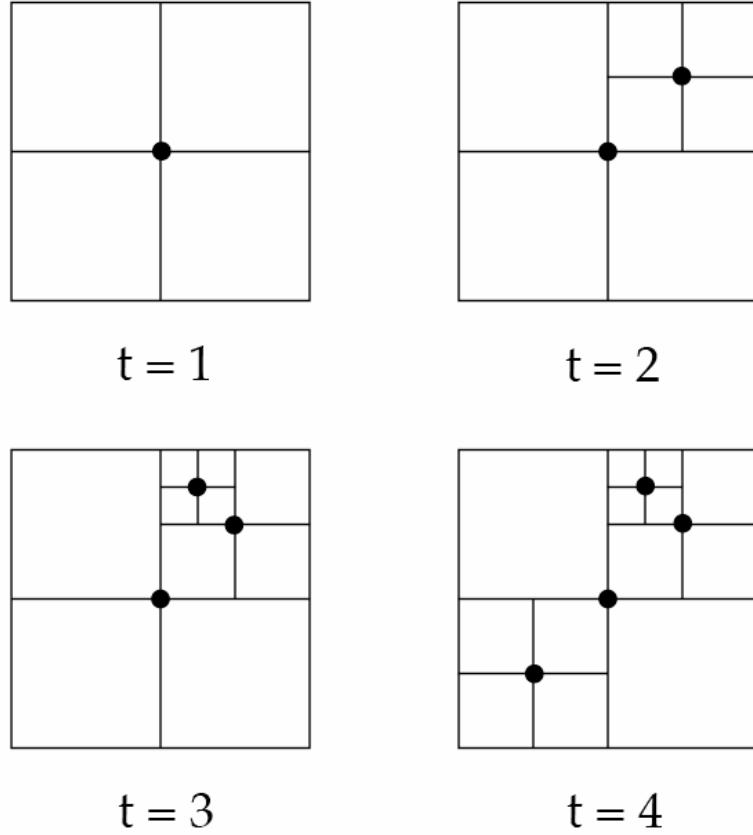


FIG. 6: Three representative steps of Models 2 and 4.

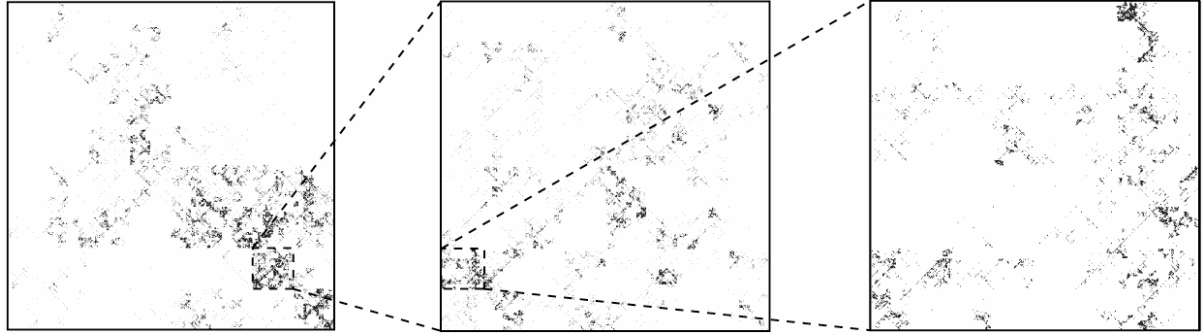


FIG. 7: A plot of a 4×10^5 point distribution on the unit square generated by Model 2. Dense regions are magnified to illustrate the heterogeneity of the point densities in the distribution at different scales.

C. 1-D Larger Interval (Model 3)

Model 3 is a one dimensional point placement model similar to Model 1, but with a different local resettlement rule. That is, the initial state and Step (a) are identical to those

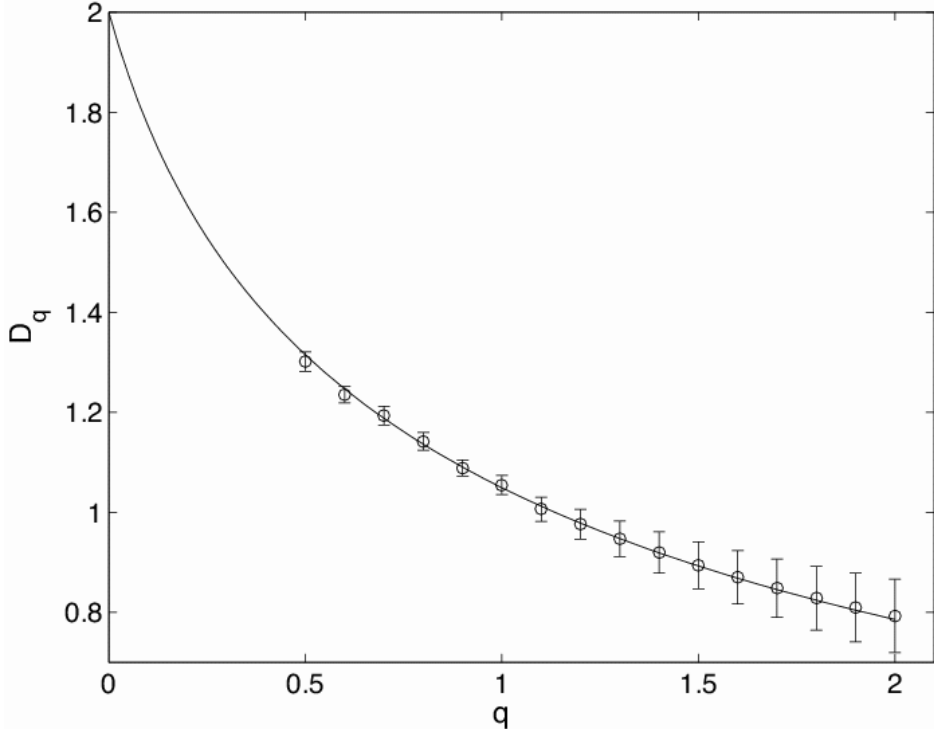


FIG. 8: Plot of D_q for Model 2. The open circles are the average numerical values of D_q (see caption in Fig. 5) obtained from 20 realizations of 10^6 point distributions generated by this model and the error bars are the sample standard deviations for each value. The solid line is the analytical result of Eq. (28).

of Model 1, while Step (b) is modified. Instead of a new point being randomly placed in one of the adjacent intervals of the chosen target point with equal probability, the new point is placed in the larger of the two intervals adjacent to the target point, and, if the two intervals are equal in size, one is chosen at random.

In this way, the new points seek out more sparsely populated local intervals to settle within. This strategy is reasonable in a context such as human resettlement, where the settlers may try to combine the convenience of being close to others with the possible advantages associated with more space. We expect this resettlement scheme to yield distributions that are more homogeneous than those created by Model 1, and hence yield greater D_q .

We plot the point location histograms for one distribution generated by this model in Fig. 9, once again varying the bin sizes used. Although the roughening of the plot as the bin size is decreased is less pronounced than what was observed in Fig. 4 for Model 1, there still appear to be significant fluctuations in the densities. We numerically obtain D_q and

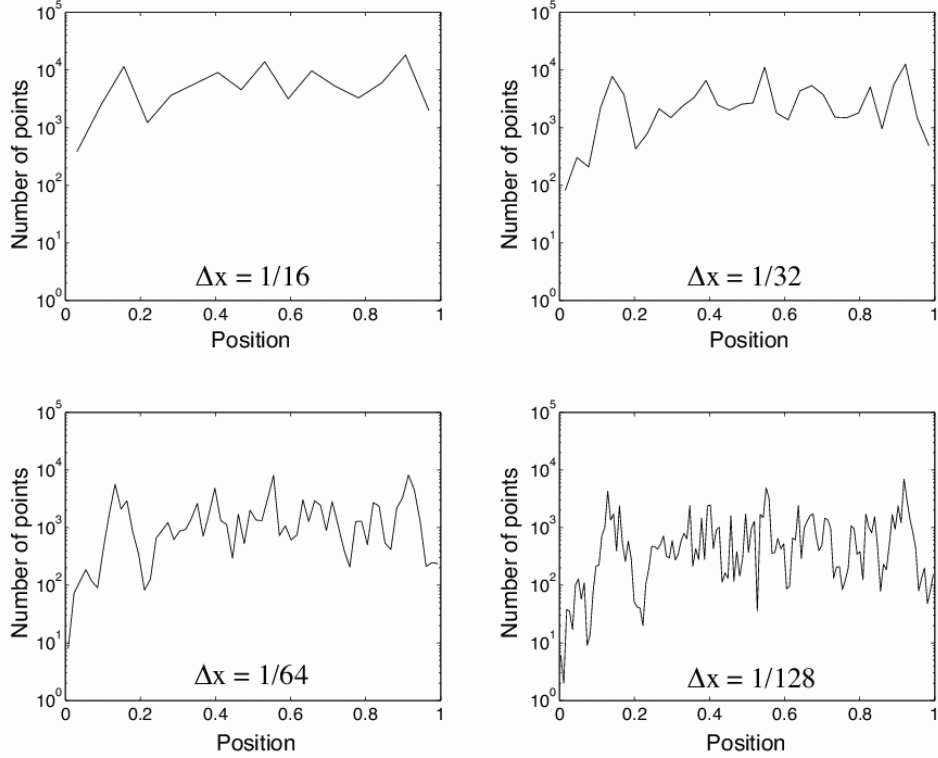


FIG. 9: Semilog plots of histograms of point locations on the unit interval for a 10^5 point distribution generated by Model 3, for various bin sizes Δx . a) $\Delta x = 1/16$, b) $\Delta x = 1/32$, c) $\Delta x = 1/64$, d) $\Delta x = 1/128$.

find the dimension spectrum to be multifractal, having the same qualitative shape as the D_q for Model 1. However, due to the more uniform nature of the distributions created by this model, the specific values of D_q are larger at each q (e.g., $D_1 = 0.84 \pm 0.01$ [averaged over 20 distributions of 10^6 points] for this model versus our analytical result $D_1 \simeq 0.72$ for Model 1 [Eq. 15]).

D. 2-D Sparse Square (Model 4)

Model 4 is a two dimensional analogue of Model 3. The initial state and Step (a) of its construction are the same as in Model 2. Our aim is to extend Step (b) of Model 3, the choosing of the larger interval for settlement, to two dimensions and for that purpose we make the following observation. In the square-based two dimensional point placement scheme of Model 2, there are two different types of squares which we refer to as type I and

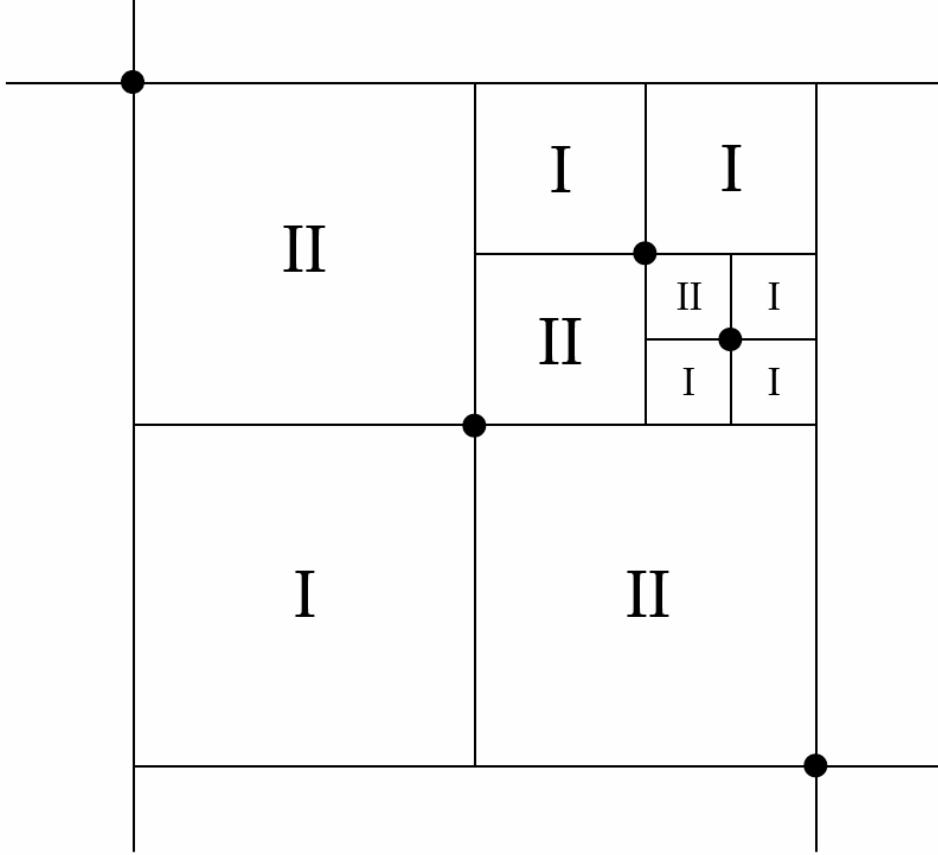


FIG. 10: Illustration of type I (labeled I) and type II (labeled II) squares, where black dots indicate populated vertices.

type II squares. A type I square only has one of its vertices occupied by a point, while a type II square has two opposite vertices occupied by points. (See Fig. 10 for an illustration of type I and type II squares.) Thus a type I square can be regarded as more sparsely populated than a type II square of equal size. With this in mind, Step (b) for Model 4 is to place the new node in the middle of the largest square adjacent to the target point. In case of a tie, choose a type I square over a type II square, with any subsequent ties being resolved by an equal probability random choice from the remaining candidate squares.

We plot a distribution generated by this model in Fig. 11. We find this distribution to be multifractal, with a D_q that is similar in shape to, but everywhere larger than, the D_q of Model 2 (except for $q = 0$ where the two coincide with $D_0 = 2$). In particular, the information dimension is $D_1 = 1.30 \pm 0.02$ (averaged over 20 distributions of 10^6 points), as compared to $D_1 \simeq 1.05$ for Model 2 (Eq. 29).

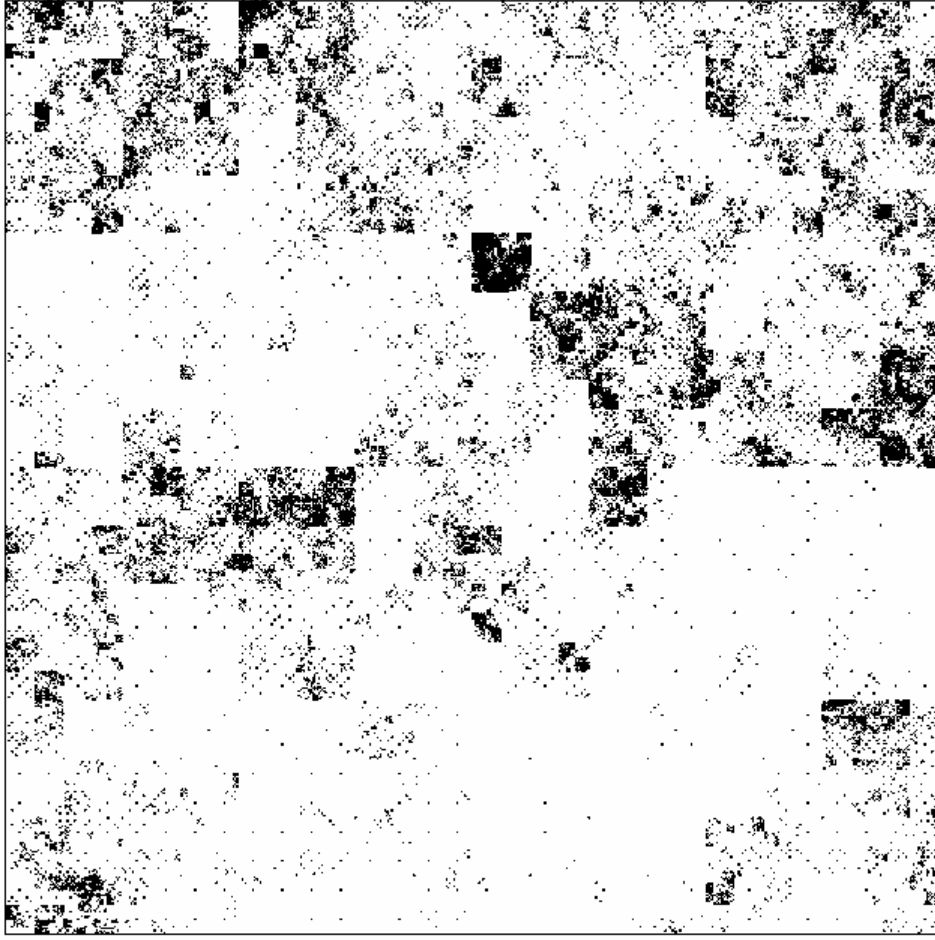


FIG. 11: A plot of a 10^5 point distribution on the unit square generated by Model 4.

E. 2-D Unstructured (Model 5)

Looking at Fig. 7 (Model 2) and Fig. 11 (Model 4), we notice square shaped artifacts and diagonal point formations that arise due to the structured, square-based nature of those point placement schemes. Model 5 is a two dimensional point placement scheme that aims to avoid such artifacts, while maintaining the two ingredients of reproduction and local resettlement. We begin with a point at $(0.5, 0.5)$ and assign to this point a *child distance* $d_c = 1/4$. Step (a) is identical to that used in Models 1-4. Once the target point is selected, Step (b) is to place the new point at a random location on the circumference of a circle centered on the target point and with radius equal to the target point's d_c . A child distance equal to half the target point's d_c is assigned to the new point.

A distribution generated by Model 5 is shown in Fig. 12. As intended, there are no grid-

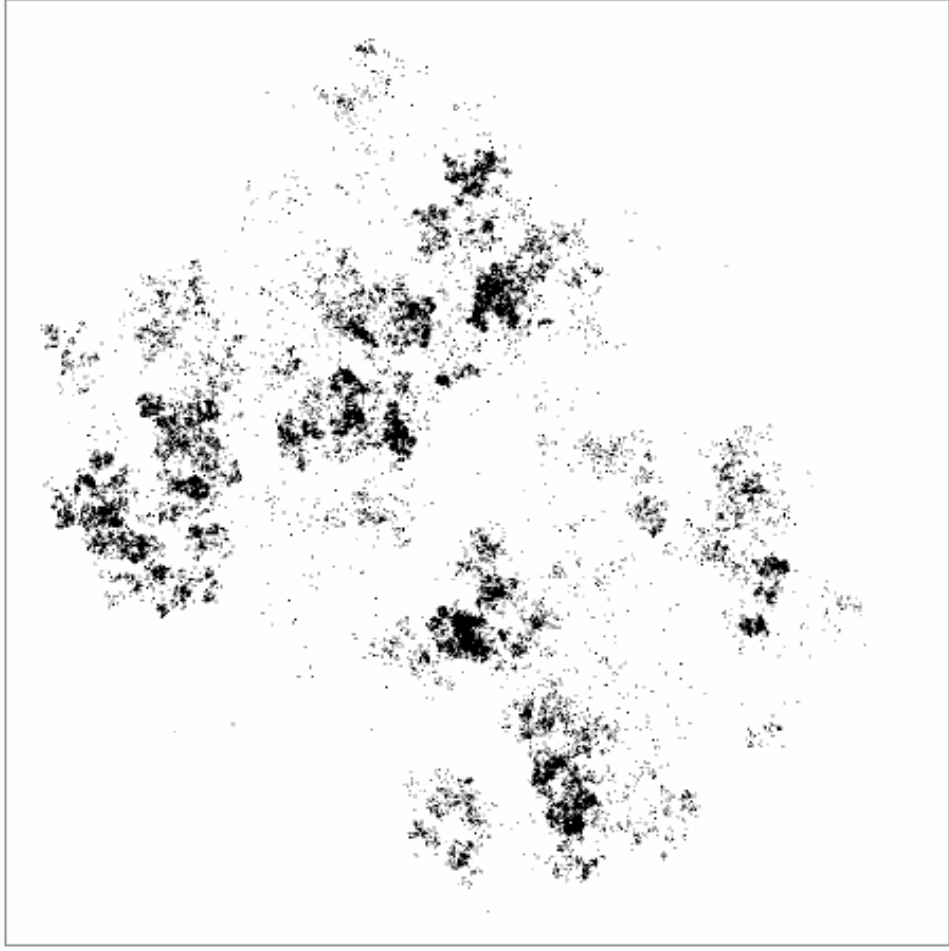


FIG. 12: A plot of a 10^5 point distribution on the unit square generated by Model 5.

type artifacts visible. The distributions generated by this model are found to be multifractal with $D_1 = 1.36 \pm 0.05$ (averaged over 20 distributions of 10^6 points).

F. 2-D Square (Model 6)

In this model we consider points to be located at the *centers* of squares. Beginning with a single point in the center of a unit edge length square, we consider reproduction by a process mimicking cell division: In Step (b) a point that was randomly chosen in Step (a) divides into four points (four-fold cell division), all of which then disperse to occupy (resettle) the centers of the four equal size squares obtained by partitioning the original square; see Fig. 13.

Note that this construction can be specified without reference to points, but only to the squares they occupy: We can consider Step (a) as randomly choosing a square with equal

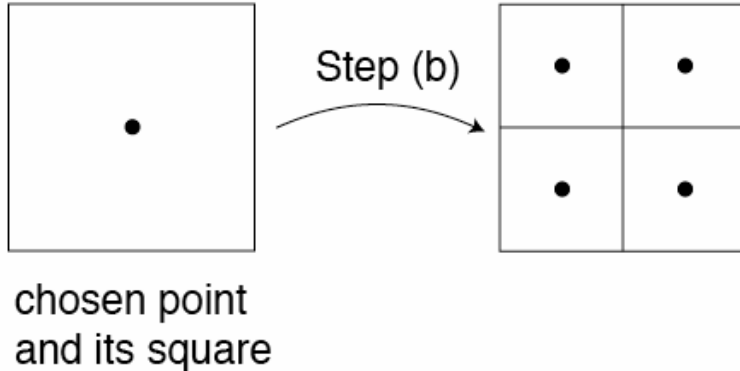


FIG. 13: Illustration of Step (b) of Model 6.

probability (independent of the size of the square), and Step (b) as dividing the chosen square into four equal new squares. After many applications of this area partitioning procedure, the corresponding population distribution can be produced by simply placing a point in the center of each square.

Figure 14 is a plot of the average D_q of 20 independent distributions generated by this model, where the solid line is the analytical result (34) derived in Sec. V C. Both the numerical and analytical results confirm that Model 6 generates multifractal distributions.

G. 2-D Triangle (Model 7)

Model 7 is a slight variation of Model 6. Here triangles, as opposed to squares, are the basis of the construction. We begin with a single equilateral triangle with unit edge length. At each time step: (a) a target point (triangle) is chosen from all the preexisting points (triangles) with equal probability; (b) the target point's triangle is divided into four identical equilateral triangles with edge length equal to half the edge length of the original triangle (see Fig. 15), with points placed in their centers. We show in Sec. V C that Model 7 has the identical analytical expression for D_q as Model 6, and thus also results in multifractal distributions.

Table I summarizes results for D_1 for our models and for the Earth at Night. Table II summarizes metaphorical interpretations of the reproduction and local resettlement characteristics of our seven models.

Our result that the different strategies of reproduction and local resettlement used in

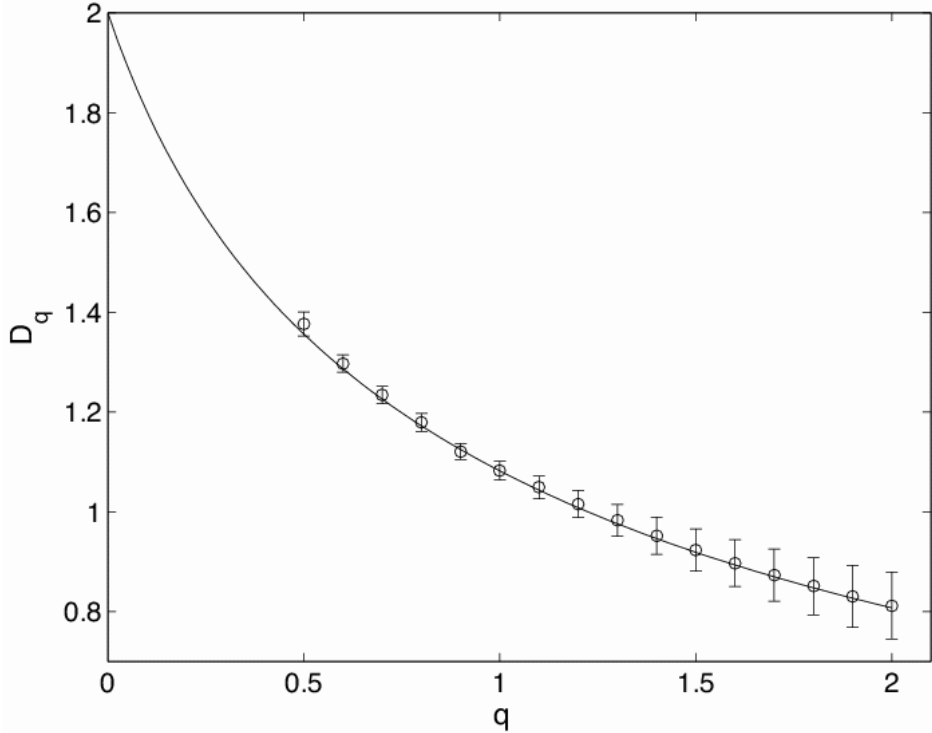


FIG. 14: Plot of D_q for Model 6. The open circles are the average numerical values of D_q (see caption in Fig. 5) obtained from 20 realizations of 10^6 point distributions generated by this model and the error bars are the sample standard deviations for each value. The solid line is the analytical result of Eq. (34).

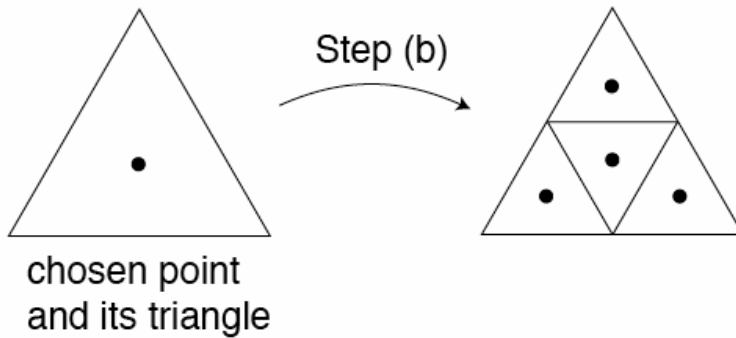


FIG. 15: Illustration of Step (b) of Model 7.

these models (Table II) all lead to multifractal spatial patterns of population density strongly suggests that multifractality may be a generic feature in real situations in which processes involving reproduction and local resettlement take place.

We emphasize that the spirit of our approach is very minimalist. In many real cases mul-

TABLE I: A summary of numerical and theoretical results for the point placement models and the Earth at Night image (Fig. 1).

Model	Dimensionality of Space	D_1	D_q (theory)
1	1	$\frac{1}{2 \ln 2} \simeq 0.72$	Eq. (14)
2	2	$\frac{8}{11 \ln 2} \simeq 1.05$	Eq. (28)
3	1	0.84 ± 0.01	-
4	2	1.30 ± 0.02	-
5	2	1.36 ± 0.05	-
6,7	2	$\frac{3}{4 \ln 2} \simeq 1.08$	Eq. (34)
Earth at Night	2	1.60 ± 0.02	-

tiple interacting complex processes undoubtedly influence the determination of population patterns. For example, several likely candidates for the EaN image are geography (mountains, rivers, deserts, etc.), politics, societal and cultural factors, economics, etc. Our models show that considerations of complex spatially heterogeneous processes are not required for explaining the existence of fractally heterogeneous distributions: even very simple dynamics incorporating reproduction and local resettlement are sufficient.

III. THE EFFECT OF CLIPPED DATA ON MULTIFRACTALITY

We now revisit the Earth at Night image (Fig. 1) and analyze its fractal properties. Figure 16(a) is a plot of D_q calculated from the measured light distribution, where the error bars indicate the uncertainty involved in extracting the slopes of the various scaling regions. One feature that is clear is that D_q appears to flatten out (i.e., there is very little variation with q) for $q > 0.8$, a characteristic not found in the D_q plots of the models we have examined in Sec. II. We now show how this discrepancy can be resolved.

Figure 17 is a log-log plot of the histogram of pixel intensities. A spike is observed for a range of intensity values near the maximum value. This suggests that some regions with high light intensities caused some of the photoelectric cells of the satellites' sensors to saturate, thereby clipping the intensity values at a maximum allowable value. Additionally, it is known that when a photoelectric cell is subjected to high intensities, it can trigger

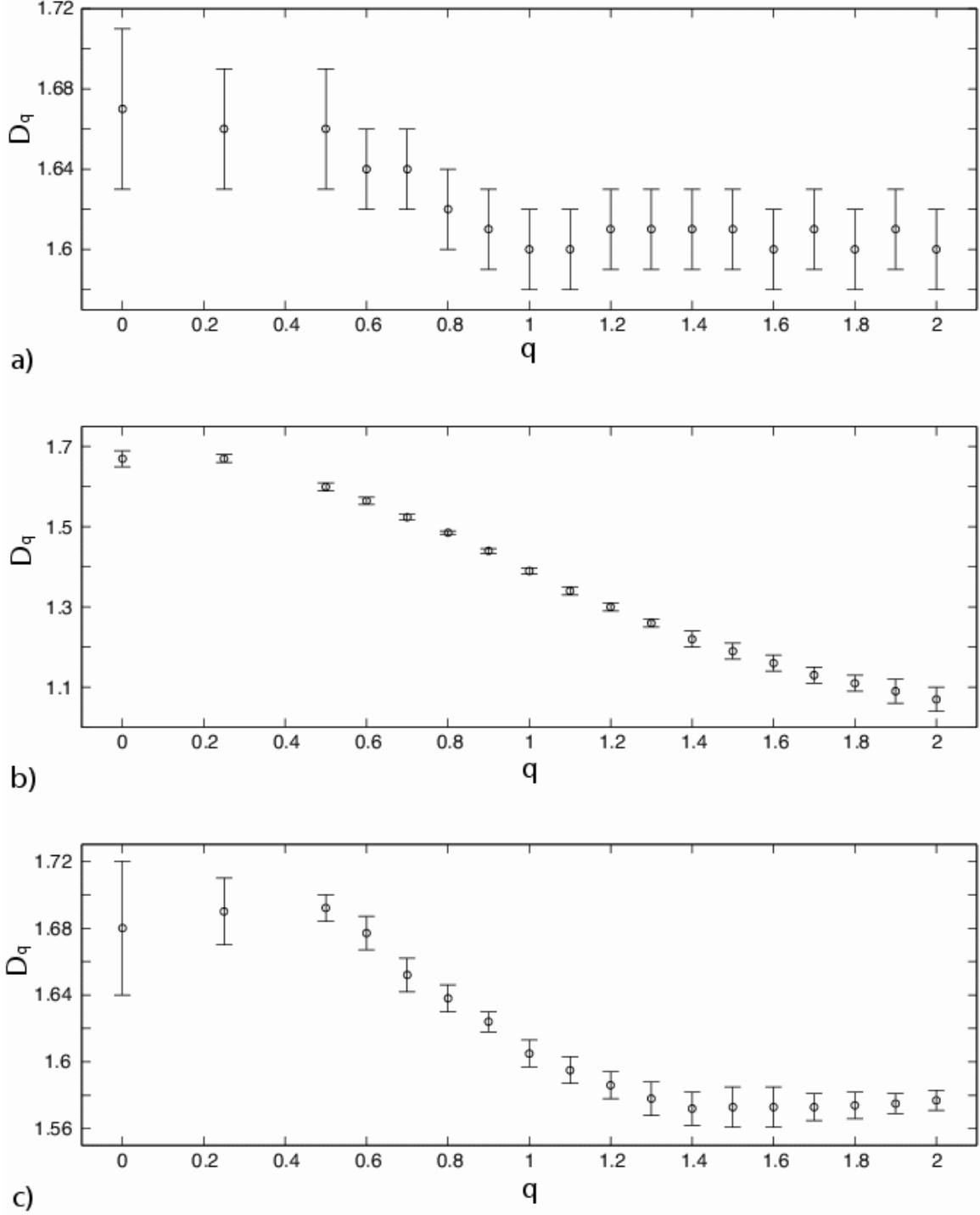


FIG. 16: a) Plot of D_q for the Earth at Night image. b) Plot of D_q for a 10^6 point distribution generated by Model 5 before the clipping procedure discussed in Section III is applied, and c) after it is applied (note the different vertical scales). The error bars reflect the uncertainty involved in determining the slopes of the scaling regions in the plots of the quantity $(1 - q)^{-1} \ln I(q, \epsilon)$ versus $\ln(1/\epsilon)$ [see Eq. (1)].

TABLE II: Summary of reproduction and local resettlement strategies employed in Models 1-7.

Model	Reproduction	Resettlement
1	parent has one child	child settles randomly chosen adjacent interval
2	parent has one child	child settles randomly chosen adjacent square
3	parent has one child	child settles largest adjacent interval
4	parent has one child	child settles largest and sparsest adjacent square
5	parent has one child	child settles in a random direction
6	parent reproduces by four-fold cell division	offspring share equally the original square area occupied by their parent
7	parent has three children	parent remains in place; offspring settle equal shares of parent's triangular area
	or	
	parent reproduces by four-fold cell division	offspring share equally the original triangular area occupied by their parent

surrounding cells to register more light, resulting in the so called “blooming” effect, which may account for the broadness of the observed spike. We note that the pixels that are part of the spike account for roughly 3% of the total number of non-zero intensity pixels and 10% of the total measured intensity (we consider any pixel with intensity value greater than 209, out of a maximum intensity value of 218, to be part of the spike).

To illustrate the effects that this type of clipping has on multifractal distributions, we apply a scheme that mimics the clipping in the EaN image to a point distribution generated by one of our models. For this purpose we choose a 10^6 point distribution generated by Model

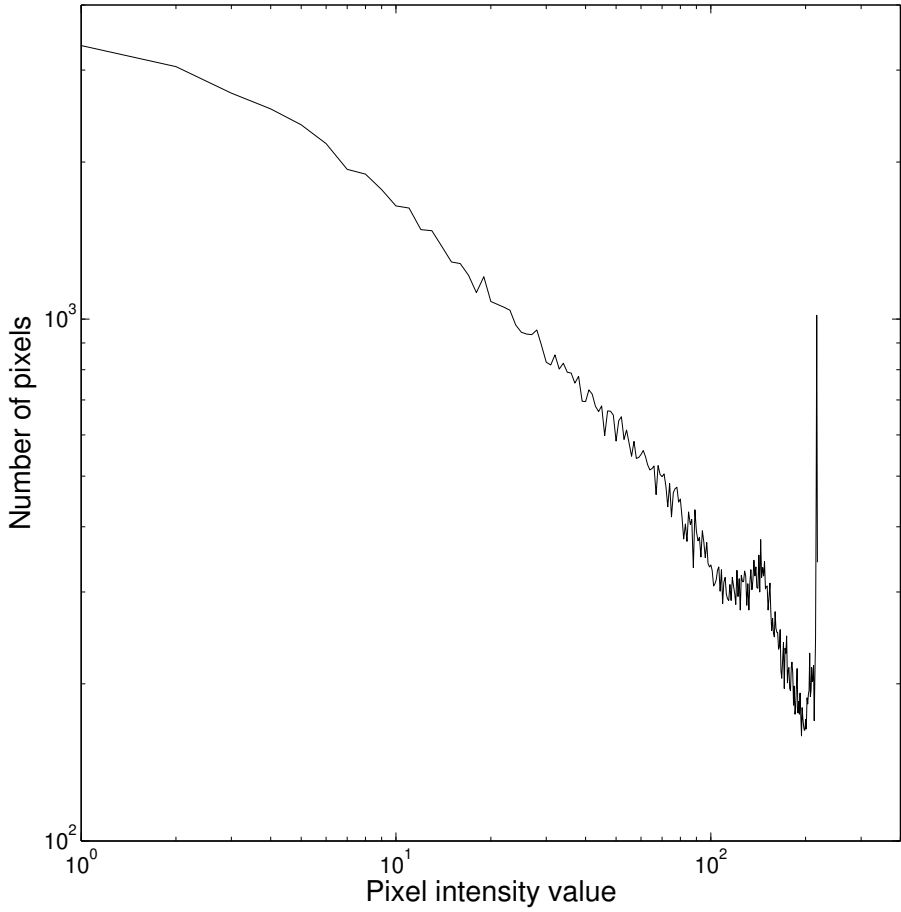


FIG. 17: Histogram of individual pixel intensities for the Earth at Night image.

5. (Similar results are obtained using our other models.) First we match the smallest scale of our distribution to that of the EaN image. Since the EaN image we analyzed is made up of 2400×800 pixels, we cover our distribution with a fixed size grid of simulated pixels in which a simulated pixel corresponds to a grid square with edge length of $1/1400 \simeq 1/\sqrt{2400 \times 800}$. Next, we choose the clipping value such that the total number of clipped simulated pixels make up 3% of the total nonempty simulated pixels. For this particular distribution, any simulated pixel containing more than 58 points has its count reset to 58.

Figures 18(a) and 18(b) are histograms showing the distribution of the number of points contained in individual simulated pixels before and after the clipping is applied, respectively. We see that the clipped histogram is qualitatively similar to the histogram for the EaN image (Fig. 17). Next, we calculate D_q for the point distribution before and after clipping

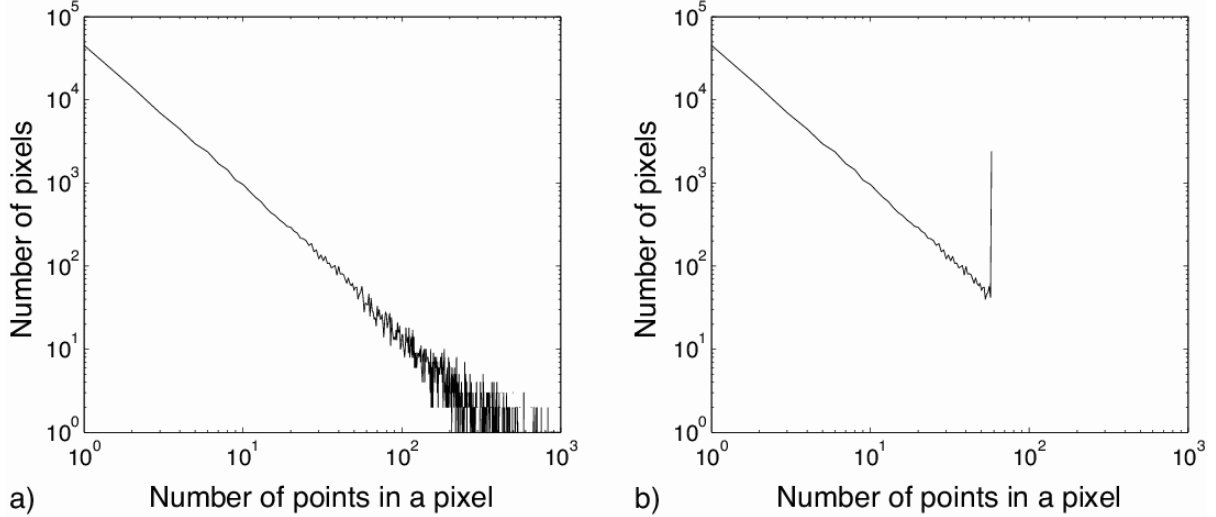


FIG. 18: Histograms of the number of points in individual simulated pixels (boxes in an $\epsilon = 1/1400$ grid) used to cover a 10^6 point distribution generated by Model 5, a) for the original distribution and b) after the original distribution was clipped by allowing a maximum of 58 points in any simulated pixel.

(Fig. 16(b) and Fig. 16(c), respectively). Noting the different vertical scales, we see that the clipping procedure transforms the D_q of Fig. 16(b) to a more gradual curve [Fig. 16(c)] with an apparent constant tail for the larger q values, making it similar to the D_q for the EaN image [Fig. 16(a)]. Additionally, we note that the value of D_1 is raised by the clipping (to approximately 1.61 from approximately 1.39). Comparing Fig. 16(a) and Fig. 16(c), we are able to conclude that the EaN image characteristics are consistent with a multifractal light intensity distribution sensed by an instrument that saturates at a maximum measurable intensity value.

IV. INHOMOGENEITY

Our models can be generalized to include geographical inhomogeneity. For example, one can imagine that the underlying space is supplemented by a fertility field, and that reproduction is more likely in regions of higher fertility. To investigate the effects of such inhomogeneities on the D_q of a point distribution, we modify Step (a) of Model 6 by use of a fertility field $F(x, y)$ which we use to construct a space-dependent, parent node selection probability. If the location of node i is (x_i, y_i) , then the selection probability for this node

is taken to be $P_i = F(x_i, y_i) / \sum_j F(x_j, y_j)$. We investigate two forms for the fertility field. First we use a smooth field

$$F_s(x, y) = 1 - 0.3 \{ \cos(2\pi x) + \sin(2\pi y) \} \quad (4)$$

on the unit square ($0 \leq x \leq 1, 0 \leq y \leq 1$). We generate point distributions with this modified version of Model 6 and find that, while the regions of larger F_s in the center of the square are much more dense with points than the regions of smaller F_s near the corners, there is, nevertheless, no discernible difference in D_q compared to the homogeneous case. That is, both the values of D_q , as well as the quality and extent of the scaling ranges, remain unchanged.

Next, to explore whether the above result can be attributed to the local smoothness of F_s , we consider a rough fertility field,

$$F_r(x, y) = 1 + 0.1 [f_w(x) + f_w(y)], \quad (5)$$

$$f_w(z) \equiv - \sum_{j=0}^{\infty} \alpha^{-j} \cos(2\pi\beta^j z). \quad (6)$$

with $\alpha = 1.5$ and $\beta = 3$. For $\alpha < \beta$, the function $f_w(z)$ is a ‘Weierstrass function’ (see Fig. 19); it is rough in the sense that, although it is continuous, it is nondifferentiable, and the graph of $f_w(z)$ versus z is a fractal curve (the fractal dimension of the curve is $2 - (\ln \alpha)/(\ln \beta) \simeq 1.63$ [8]). With $\alpha = 1.5$, F_r has the same range of variation as F_s (i.e., 0.4 to 1.6). Applying this fertility field to Model 6 results in the same values and scaling ranges for D_q as in the homogeneous case and the smooth fertility field case [Eq. (4)]. This suggests that, while inhomogeneities of the underlying space may dictate certain aspects of the distribution of a growing population, for example, where the points are more likely to settle, its fractality can be due mainly to reproduction and local resettlement processes.

V. THEORY

A. Model 1

Here we derive an analytical expression for the fractal dimension spectrum D_q of population distributions generated by the one dimensional point placement scheme of Model 1. We begin by making the following observation. Choosing a target interval by first selecting a target point from all the preexisting points with equal probability and then selecting

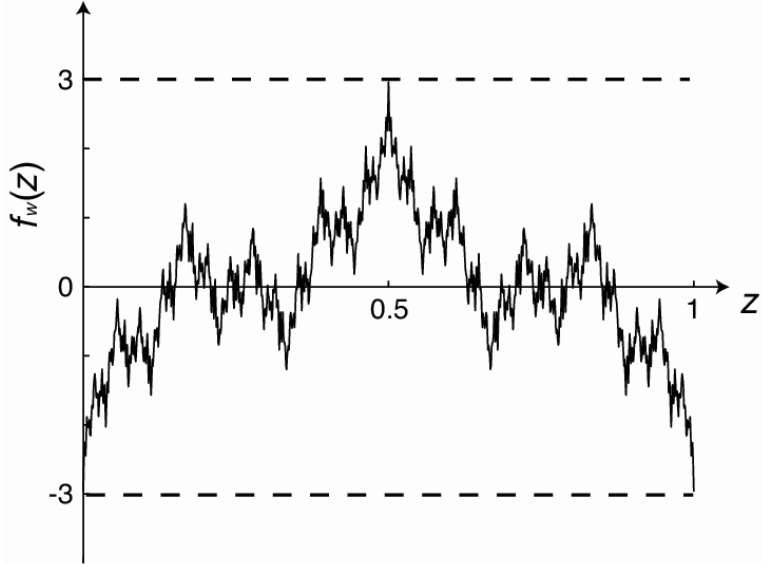


FIG. 19: A plot of the Weierstrass function $f_w(z)$ [Eq. (6)]. In our numerical implementation the infinite upper limit on the summation in Eq. (6) is replaced by j_{max} , where j_{max} is chosen such that the smallest value of ϵ used in determining D_q is at least one order of magnitude larger than the smallest scale of the roughness, $3^{-j_{max}}$.

between the two adjacent intervals of the target point with equal probability is equivalent to choosing a target interval out of all the preexisting intervals with equal probability, up to the negligible effect (for large time) of the edge intervals that are only bounded on one of their sides by a point. (Alternatively, one could impose periodic boundary conditions on the unit interval, which would result in complete equivalence of the two constructions.)

Having made this identification, we define $N(k, t)$ to be the average (over different realizations of Model 1) number of intervals of length 2^{-k} at time t , where at every integer value of t a new point is added. The initial condition for this model (at $t = 1$) is a single point at $x = 0.5$ on the unit interval ($0 \leq x \leq 1$). This defines two intervals of length $1/2$ and thus $N(k, 1) = 2\delta_{k1}$, where δ_{kj} is the Kronecker delta. At each time t , the probability that an interval of length 2^{-k} is chosen is $N(k, t) / \sum_j N(j, t)$. Then, in place of such a chosen interval, two intervals of length $2^{-(k+1)}$ are created. Since we begin with two intervals at $t = 1$ and at each subsequent time step an interval is destroyed while two are newly created, we see that $\sum_j N(j, t) = t + 1$. The discrete time evolution equation for N is then

$$N(k, t+1) = \left(1 - \frac{1}{t+1}\right) N(k, t) + \frac{2}{t+1} N(k-1, t), \quad (7)$$

where $1/(t+1)$ is the probability that a given interval is selected at time t , $(t+1)^{-1}N(k,t)$ is the average (over different realizations of Model 1) number of intervals of length 2^{-k} destroyed at time $t+1$, and $2(t+1)^{-1}N(k-1,t)$ is the average number of 2^{-k} length intervals created at time $t+1$. Alternatively, in terms of $n(k,t)$, the fraction of the total number of intervals at time t with length 2^{-k} , given by $n(k,t) = N(k,t)/(t+1)$, the evolution equation is

$$n(k,t+1) = \left(\frac{t}{t+2}\right)n(k,t) + \left(\frac{2}{t+2}\right)n(k-1,t). \quad (8)$$

In Appendix A, we introduce the partition function formalism for calculating D_q . We define the quantity $\tau = (q-1)D_q$ and derive the following expression for $q(\tau)$ for Model 1 [Eq. (A10)]:

$$q(\tau) = 1 + \lim_{t \rightarrow \infty} \frac{\ln \langle 2^{k\tau} \rangle_t}{\ln t}, \quad \langle 2^{k\tau} \rangle_t = \sum_k n(k,t) 2^{k\tau}. \quad (9)$$

Multiplying both sides of Eq. (8) by $2^{k\tau}$ and then summing over k , we obtain the recursion relation,

$$\langle 2^{k\tau} \rangle_{t+1} = \langle 2^{k\tau} \rangle_t \left(1 + \frac{2^{\tau+1} - 2}{t+2}\right), \quad (10)$$

which, since $\langle 2^{k\tau} \rangle_{t=1} = 2^\tau$, can be solved to yield,

$$\langle 2^{k\tau} \rangle_t = \prod_{i=1}^t \left(1 + \frac{2^{\tau+1} - 2}{i+1}\right). \quad (11)$$

Substituting Eq. (11) into Eq. (9), we obtain

$$q = 2^{\tau+1} - 1, \quad (12)$$

where we have made use of the relationship

$$\lim_{t \rightarrow \infty} \frac{\sum_{i=a}^t \ln \left(1 + \frac{x}{i+y}\right)}{\ln t} = x, \quad (13)$$

for x and y constants and a an integer such that $a+y+x > 0$ and $a+y > 0$. Then, since $D_q = \tau(q)/(q-1)$, we invert Eq. (12) for $\tau(q)$ and obtain the following result for D_q :

$$D_q = \frac{\log_2(q+1) - 1}{q-1}. \quad (14)$$

In particular, using L'Hospital's Rule,

$$D_1 = \frac{1}{2 \ln 2} \simeq 0.72. \quad (15)$$

B. Model 2

The calculation of D_q for Model 2 is based on the classification of squares into types I and II, discussed in Sec. II D. We begin by defining $N_1(k, t)$ and $N_2(k, t)$ to be the average (over different realizations) number of type I and type II squares, respectively, with edge length 2^{-k} at time t . The initial state ($t = 1$) is a single point at $(0.5, 0.5)$. The point divides the unit square into four equal squares of edge length $1/2$, with each square having one point on one of its vertices. Thus $N_1(k, 1) = 4\delta_{k1}$, while $N_2(k, 1) = 0$ for all k . At each time t , the new point is equally likely to appear in each type I square, but is twice as likely to appear in each type II square, because there are two parent points that can produce offspring in each type II square. In other words, a type I square with edge length 2^{-k} is chosen with probability $N_1(k, t)/\sum_j (N_1(j, t) + 2N_2(j, t))$, while a type II square of the same size is chosen with probability $2N_2(k, t)/\sum_j (N_1(j, t) + 2N_2(j, t))$. When a type I square is chosen, the new point is placed in its center, destroying the original square and creating three type I squares and one type II square, all with half the edge length of the original square. On the other hand, when the new point is in a type II square, it is replaced by two type I squares and two type II squares, all having half the edge length of the original square. Notice that either way, the quantity $\sum_j (N_1(j, t) + 2N_2(j, t))$ increases by 4 between time t and $t + 1$, so that $\sum_j (N_1(j, t) + 2N_2(j, t)) = 4t$.

The discrete time evolution equations for both types of squares are then

$$N_1(k, t + 1) = N_1(k, t) \left(1 - \frac{1}{4t}\right) + N_1(k - 1, t) \frac{3}{4t} + N_2(k - 1, t) \frac{4}{4t}, \quad (16)$$

$$N_2(k, t + 1) = N_2(k, t) \left(1 - \frac{2}{4t}\right) + N_1(k - 1, t) \frac{1}{4t} + N_2(k - 1, t) \frac{4}{4t}. \quad (17)$$

In Appendix A we show that for Model 2 [Eq. (A12)],

$$q(\tau) = \lim_{t \rightarrow \infty} \frac{\ln (T_1(t) + 2^q T_2(t))}{\ln t}, \quad (18)$$

where $T_i(t) = \sum_k 2^{k\tau} N_i(k, t)$. Multiplying Eqs. (16) and (17) by $2^{k\tau}$ and summing over k , we obtain

$$T_1(t + 1) = T_1(t) \left(1 + \frac{3 \cdot 2^\tau - 1}{4t}\right) + T_2(t) \frac{4 \cdot 2^\tau}{4t}, \quad (19)$$

$$T_2(t + 1) = T_2(t) \left(1 + \frac{4 \cdot 2^\tau - 2}{4t}\right) + T_1(t) \frac{2^\tau}{4t}. \quad (20)$$

At this point, we make the continuous time approximation $T_i(t+1) - T_i(t) \approx dT_i(t)/dt$, valid for large t , which allows us to represent Eqs. (19) and (20) as the matrix differential equation,

$$\frac{d\mathbf{T}(s)}{ds} = \mathbf{M} \cdot \mathbf{T}(s), \quad (21)$$

where

$$\mathbf{T}(s) = \begin{bmatrix} T_1(s) \\ T_2(s) \end{bmatrix}, \quad (22)$$

$$\mathbf{M} = \begin{bmatrix} 3 \cdot 2^\tau - 1 & 4 \cdot 2^\tau \\ 2^\tau & 4 \cdot 2^\tau - 2 \end{bmatrix} \quad (23)$$

and $s = (1/4) \ln t$.

Equation (21) is solved in terms of the eigenvalues λ_a, λ_b and the eigenvectors $\mathbf{T}_a, \mathbf{T}_b$ of the matrix \mathbf{M} , giving

$$\mathbf{T}_i \sim e^{\lambda_i s} = t^{\frac{\lambda_i}{4}}, \quad (24)$$

for $i = a, b$, with λ_a, λ_b distinct and real and $\lambda_a > \lambda_b$. We can express the quantity $(T_1(t) + 2^q T_2(t))$ in Eq. (18) in terms of a linear combination of the components of these eigenvectors, whose long time behavior is dominated by the behavior of \mathbf{T}_a , the eigenvector associated with the larger eigenvalue λ_a . Thus (18) gives us the simple result

$$q = \lambda_a/4. \quad (25)$$

The eigenvalues of \mathbf{M} are the roots of its characteristic polynomial,

$$\lambda^2 + \lambda(3 - 7 \cdot 2^\tau) + 2 - 10 \cdot 2^\tau + 8 \cdot 2^{2\tau} = 0. \quad (26)$$

This equation is also quadratic in 2^τ , allowing us to solve for $\tau(\lambda)$

$$\tau(\lambda) = \log_2 \left[\frac{1}{16} \left(10 + 7\lambda \pm \sqrt{17\lambda^2 + 44\lambda + 36} \right) \right]. \quad (27)$$

We substitute the relationship from Eq. (25) into Eq. (27) and, since $\tau(q) = (q-1)D_q$, we resolve the ambiguity of the \pm sign by requiring that $\tau(q=1) = 0$. This results in

$$D_q = \frac{1}{q-1} \log_2 \left[\frac{1}{8} \left(5 + 14q - \sqrt{68q^2 + 44q + 9} \right) \right] \quad (28)$$

for the dimension spectrum of Model 2. In particular, applying L'Hospital's Rule to (28), the information dimension is

$$D_1 = \frac{8}{11 \ln 2} \simeq 1.05. \quad (29)$$

C. Models 6 and 7

Although Model 6 is a two dimensional point placement scheme, the fact that each square is equally likely to be chosen at a given time allows the calculation of D_q to be very similar to that for the one dimensional scheme of Model 1. We begin by defining $N(k, t)$ to be the average number of squares with edge length 2^{-k} at time t . The initial state (at $t = 1$) is a single square with unit edge length, giving us $N(k, 1) = \delta_{k0}$. At each time t , a square with edge length 2^{-k} is chosen with probability $N(k, t) / \sum_j N(j, t)$ and replaced by four equal squares with edge lengths $2^{-(k+1)}$. Since at each time step there is a net gain of three squares, we see that $\sum_j N(j, t) = 3t - 2$, and obtain the following discrete time evolution equation for N :

$$N(k, t + 1) = N(k, t) \left(1 - \frac{1}{3t - 2}\right) + N(k - 1, t) \frac{4}{3t - 2}. \quad (30)$$

In terms of the fraction $n(k, t) = N(k, t) / (3t - 2)$ of squares with edge length 2^{-k} , we have

$$n(k, t + 1) = n(k, t) \frac{3t - 3}{3t + 1} + n(k - 1, t) \frac{4}{3t + 1}. \quad (31)$$

Interchanging the squares in the above derivation with equilateral triangles, one can see that the same evolution equations hold for the triangles in Model 7.

In Appendix A we show that Eq. (9), which allowed us to calculate $q(\tau)$ in terms of $\langle 2^{k\tau} \rangle_t$ for Model 1, holds for Models 6 and 7 as well. Following the procedure in Section V A, we multiply both sides of Eq. (31) by $2^{k\tau}$ and sum over k , solving the resulting recursion relation to obtain

$$\langle 2^{k\tau} \rangle_t = \prod_{i=2}^t \left(1 + \frac{(2^\tau - 1) 4/3}{i - 2/3}\right). \quad (32)$$

Making use of the relationship in Eq. (13), we get

$$q(\tau) = 1 + \frac{4}{3} (2^\tau - 1). \quad (33)$$

This equation is inverted to solve for $\tau(q)$ which, when divided by $(q - 1)$, gives us the multifractal dimension spectrum

$$D_q = \frac{\log_2 \left((q - 1) \frac{3}{4} + 1 \right)}{q - 1}. \quad (34)$$

The information dimension is

$$D_1 = \frac{3}{4 \log 2} \simeq 1.08. \quad (35)$$

VI. CONCLUSION

The main conclusion of this paper is that reproduction and local resettlement processes may lead to multifractal spatial distributions for growing populations. We introduced a number of point placement models in one and two dimensions and showed that the models resulted in multifractal distributions. Furthermore, we have demonstrated qualitative similarity between the example of the Earth at Night image and clipped versions of distributions generated by our models. We thus suggest that the mechanism by which our models create multifractal distributions may be operative in the growth of real systems.

We thank Dan Lathrop and Rowena Ball for useful conversations. This work was supported by ONR (Physics) and by NSF (Contract Nos. PHYS 0098632 and DMS 0104087).

APPENDIX A: CALCULATION OF MODEL DIMENSION SPECTRA

1. The Partition Function Formalism

The partition function formalism [9, 10] is an alternative to the fixed sized grid method of Eq. (1) for calculating a dimension spectrum of a measure. We demonstrate here how it allows us to relate the various interval and square size distribution functions found in Models 1, 2, 6 and 7 to the dimensions of the point distributions generated by them.

We cover the measure of interest with a disjoint covering $\{S_i\}$, $i = 1, 2 \dots N$, where each element S_i of the covering set has a diameter ϵ_i less than or equal to δ . (The diameter ϵ_i is the largest possible distance between two points in S_i .) The partition function is defined as

$$\Gamma_q(\tau, \{S_i\}, \delta) = \sum_{i=1}^N \mu_i^q / \epsilon_i^\tau, \quad (\text{A1})$$

where μ_i is the measure of S_i . For a given δ the covering $\{S_i\}$ is now chosen such that Eq. (A1) is maximized (for $q > 1$) or minimized (for $q < 1$), which defines

$$\Gamma_q(\tau, \delta) = \begin{cases} \sup_{S_i} \Gamma_q(\tau, \{S_i\}, \delta), & \text{for } q > 1 \\ \inf_{S_i} \Gamma_q(\tau, \{S_i\}, \delta), & \text{for } q < 1 \end{cases} \quad (\text{A2})$$

Then, letting $\delta \rightarrow 0$, we define

$$\Gamma_q(\tau) = \lim_{\delta \rightarrow 0} \Gamma_q(\tau, \delta). \quad (\text{A3})$$

The quantity $\Gamma_q(\tau)$ experiences a jump from 0 to $+\infty$, as τ is increased, at a critical value that we denote $\tau(q)$. The dimension \tilde{D}_q of the measure is then defined as

$$\tilde{D}_q = \tau(q)/(q-1). \quad (\text{A4})$$

In practice, it is difficult to determine whether a particular covering $\{S_i\}$ is optimal in the sense of Eq. (A2). However, one can often compute the correct dimension by considering specific coverings, in the following sense. Consider a sequence of disjoint coverings $\{S_i^{(m)}\}$ where covering m of the sequence has maximum diameter $\delta^{(m)}$ ($\epsilon_i^{(m)} < \delta^{(m)}$ for every component i of covering m), and $\delta^{(m)}$ converges to zero as m approaches infinity. If the limit

$$\hat{\Gamma}_q(\tau) = \lim_{m \rightarrow \infty} \Gamma_q(\tau, \{S_i^{(m)}\}, \delta^{(m)}) \quad (\text{A5})$$

exists, then like $\Gamma_q(\tau)$ it experiences a jump from 0 to $+\infty$, as τ increases, at a critical value $\tau = \hat{\tau}(q)$. In terms of the sequence $\{S_i^{(m)}\}$ of coverings (not necessarily optimal), we can

then compute a dimension spectrum

$$\hat{D}_q = \hat{\tau}(q)/(q-1), \quad (\text{A6})$$

Since the sequence of coverings used to compute \hat{D}_q may be suboptimal, we have $\hat{\tau}(q) \geq \tau(q)$ for $q > 1$, and $\hat{\tau}(q) \leq \tau(q)$ for $q < 1$. Thus $\hat{D}_q \geq \tilde{D}_q$ in each case. Assuming the limit in Eq. (1) that defines D_q to exist, then D_q can be computed by the partition function formalism above using equal size coverings ($\epsilon_i^{(m)} = \delta^{(m)}$ for every i and m). Thus $D_q \geq \tilde{D}_q$ as well. While there do exist examples for which $\tilde{D}_q \neq D_q$ for $q < 1$ [12] the two dimensions are typically found to coincide in analytical examples with physical bases. Furthermore, for $q > 1$ the two dimensions always coincide:

Theorem: For every probability measure μ for which the limit in Eq. (1) exists, $\tilde{D}_q = D_q$ for all $q > 1$. (If one defines D_q as a liminf, then this equality holds for all μ .)

We prove this theorem in Appendix B.

The theorem demonstrates that, for $q > 1$ at least, the dimension spectrum computed according to the partition function formalism from a particular sequence of coverings is not that sensitive to the type of covering; equal size coverings yield the same spectrum as a sequence of coverings that is optimal in the sense of Eq. (A2). While it may be possible to compute a different value of \hat{D}_q from a sufficiently suboptimal sequence of coverings, we conjecture that for the coverings we consider below,

$$\hat{D}_q = \tilde{D}_q = D_q. \quad (\text{A7})$$

Furthermore, we conjecture that Eq. (A7) holds not only for $q > 1$, but for all $q \geq 0$.

For our purposes, the application of Eq. (A7) for $q \leq 1$ is supported by the following reasoning. In all of the cases below, the formula we obtain for \hat{D}_q is a complex analytic function of q . If $\hat{D}_q = D_q$ for $q > 1$, it follows that if D_q is continuous at $q = 1$, then $\hat{D}_1 = D_1$. Furthermore, if D_q is complex analytic, then $\hat{D}_q = D_q$ for $q < 1$ as well.

2. Application to the Models

The practical implication of Eq. (A7) for us is significant. It means that we can choose any sequence of coverings whose maximum diameter converges to zero, and this choice can be made in a manner that *facilitates analytic computations*. The result will be the same as that for an equal cube size covering [Eq. (1)] or an optimal covering [Eq. (A2)].

For Model 1, we choose the intervals between the points as the covering for the distribution. We regard each interval as covering the equivalent of one point since it contains two half points at each of its ends. Hence $\mu_i = (\sum_k N(k, t))^{-1} = 1/t$ for all i , and Eq. (A5) becomes

$$\hat{\Gamma}_q(\tau) = \lim_{t \rightarrow \infty} (1/t)^q \sum_{i=1}^t \epsilon_i^{-\tau}, \quad (\text{A8})$$

where the $\delta \rightarrow 0$ limit is replaced by $t \rightarrow \infty$, since, as t increases the size of the largest interval decreases to zero. Since $\ln \hat{\Gamma}_q(\tau) = -\infty$ for $\tau < \hat{\tau}(q)$ and $\ln \hat{\Gamma}_q(\tau) = \infty$ for $\tau > \hat{\tau}(q)$, we equate $\ln \hat{\Gamma}_q(\tau)$ to zero and obtain q as a function of the transition value $\hat{\tau}$,

$$q(\hat{\tau}) = \lim_{t \rightarrow \infty} \frac{\ln \sum_{i=1}^t \epsilon_i^{-\hat{\tau}}}{\ln t}. \quad (\text{A9})$$

In terms of $n(k, t)$, the fraction of the total number of intervals at time t with length 2^{-k} , we then have [see Eq. (9)]

$$q(\hat{\tau}) = 1 + \lim_{t \rightarrow \infty} \frac{\ln \langle 2^{k\hat{\tau}} \rangle_t}{\ln t}. \quad (\text{A10})$$

For Model 2 we use the two types of squares (type I and II) to cover the distribution. A type I square has one point on one of its vertices and hence covers the equivalent of a quarter of a point, while a type II square, with two points on its vertices, covers the equivalent of half a point. Thus at time t , the measure contained in a type I square is $1/4t$, while that contained in a type II square is $1/2t$. Thus Eq. (A5) becomes

$$\hat{\Gamma}_q(\tau) = \lim_{t \rightarrow \infty} \frac{1}{(4t)^q} \left(\sum_{i=1}^{N_1} \epsilon_i^{-\tau} + 2^q \sum_{i=1}^{N_2} \epsilon_i^{-\tau} \right), \quad (\text{A11})$$

where the first summation is over all type I squares and the second is over all type II squares. Taking the logarithm of this expression and equating it to zero, we obtain

$$q(\hat{\tau}) = \lim_{t \rightarrow \infty} \frac{\ln (T_1(t) + 2^q T_2(t))}{\ln t}, \quad (\text{A12})$$

where $T_i(t) = \sum_k 2^{k\hat{\tau}} N_i(k, t)$.

Each square in Model 6 and triangle in Model 7 contains $(\sum_k N(k, t))^{-1} = 1/(3t - 2)$ of the total measure. Thus, Eq. (A5) becomes

$$\hat{\Gamma}_q(\tau) = \lim_{t \rightarrow \infty} \frac{1}{(3t - 2)^q} \sum_{i=1}^{3t-2} \epsilon_i^{-\tau}. \quad (\text{A13})$$

We see that this yields an expression for $q(\hat{\tau})$ identical to that for Model 1 [Eq. (A10)].

APPENDIX B: PROOF OF THEOREM FROM APPENDIX A

As we noted in Appendix A, $\tilde{D}_q \leq D_q$ for all $q \geq 0$, so we now show that also $\tilde{D}_q \geq D_q$ for $q > 1$. Our proof is based on the theorem in [11] that for $q > 1$, the quantity

$$I_q(s) = \int \left(\int \frac{d\mu(y)}{|x-y|^s} \right)^{q-1} d\mu(x) \quad (\text{B1})$$

is finite for $s < D_q$ and infinite for $s > D_q$. To see that $\tilde{D}_q \geq D_q$, we show that $\tilde{D}_q \geq s$ whenever $I_q(s)$ is finite. Let $\{S_i\}$ be a disjoint covering of μ , as in Appendix A, and recall that μ_i is the measure of S_i and ϵ_i is its diameter. Then considering only the contribution to $I_q(s)$ from points x and y that are in the same S_i , we have

$$\begin{aligned} I_q(s) &\geq \sum_{i=1}^N \int_{S_i} \left(\int_{S_i} \frac{d\mu(y)}{|x-y|^s} \right)^{q-1} d\mu(x) \\ &\geq \sum_{i=1}^N \int_{S_i} \left(\int_{S_i} \frac{d\mu(y)}{\epsilon_i^s} \right)^{q-1} d\mu(x) \\ &= \sum_{i=1}^N \mu_i \left(\frac{\mu_i}{\epsilon_i^s} \right)^{q-1} \\ &= \sum_{i=1}^N \mu_i^q / \epsilon_i^{(q-1)s} \\ &= \Gamma_q((q-1)s, \{S_i\}, \delta) \end{aligned}$$

by (A1). This implies that $\Gamma_q((q-1)s, \delta) \leq I_q(s)$ by (A2), since $q > 1$, and hence $\Gamma_q((q-1)s) \leq I_q(s)$ by (A3). Therefore if $I_q(s)$ is finite, then $\Gamma_q((q-1)s)$ is finite, whence $\tau(q) \geq (q-1)s$, and finally $\tilde{D}_q \geq s$ by (A4).

- [1] C. Mayhew and R. Simmon, *Astronomy picture of the day: Earth at night*, URL <http://antwrp.gsfc.nasa.gov/apod/ap040822.html>.
- [2] H. Hentschel and I. Procaccia, *Physica D* **8**, 435 (1983).
- [3] P. Grassberger, *Phys. Lett. A* **97**, 227 (1983).
- [4] S. Yook, H. Jeong, and A. Barabási, *PNAS* **99**, 13382 (2002).
- [5] M. Batty and P. Longley, *Fractal Cities* (Academic Press, San Diego, 1994).
- [6] H. A. Makse, S. Havlin, and H. E. Stanley, *Nature* **377**, 608 (1995).
- [7] S. C. Manrubia, D. H. Zanette, and R. V. Solé, *Fractals* **7**, 1 (1999).

[8] E. Ott, *Chaos in Dynamical Systems* (Cambridge University Press, Cambridge, 2002), 2nd ed.

[9] P. Grassberger, Phys. Lett. A **107**, 101 (1985).

[10] T. Halsey, M. Jensen, L. Kadanoff, I. Procaccia, and B. Shraiman, Phys. Rev. A **33**, 1141 (1986).

[11] B. Hunt and V. Y. Kaloshin, Nonlinearity **10**, 1031 (1997).

[12] As a simple example, we consider the set, $1, 1/2, 1/3, \dots, n^{-1}, \dots$, and $q = 0$. For this set it can be shown that Eqs. (A1)-(A4), yield $\tilde{D}_0 = 0$, which is intuitively reasonable for a set that is a countable collection of points. In contrast, Eqs. (1) and (2) yield $D_0 = 1/2$. To see this we first note that, for $q = 0$, (1) and (2) give the well-known result $D_0 = \lim_{\epsilon \rightarrow 0} \{ [\ln N(\epsilon)] / [\ln(1/\epsilon)] \}$, where $N(\epsilon)$ is the number of ϵ -intervals needed to cover the set. Next we observe that the distance between $1/n$ and $1/(n+1)$ is approximately $1/n^2$ for large n . Thus setting $\epsilon = 1/n^2$, we need n intervals to cover the first n elements of the set, one interval for each such element. To cover the remaining elements we must cover the interval $(1/(n+1), 0)$. This requires $(1/\epsilon)[1/(n+1)] = n^2/(n+1) \simeq n$ intervals. Thus $N(\epsilon) \simeq 2n = 2/\epsilon^{1/2}$, yielding $D_0 = 1/2$.